The release of trapped gases from amorphous solid water films. II. "Bottom-up" induced desorption pathways

R. Alan May, R. Scott Smith, and Bruce D. Kay

The release of trapped gases from amorphous solid water films. II. "Bottom-up" induced desorption pathways

R. Alan May, R. Scott Smith,[a] and Bruce D. Kay[a]
Fundamental and Computational Sciences Directorate, Pacific Northwest National Laboratory, Richland, Washington 99352, USA

In this (Paper II) and the preceding companion paper (Paper I; R. May, R. Smith, and B. Kay, J. Chem. Phys. **138**, 104501 (2013)), we investigate the mechanisms for the release of trapped gases from underneath amorphous solid water (ASW) films. In Paper I, we focused on the low coverage regime where the release mechanism is controlled by crystallization-induced cracks formed in the ASW overlayer. In that regime, the results were largely independent of the particular gas underlayer. Here in Paper II, we focus on the high coverage regime where new desorption pathways become accessible prior to ASW crystallization. In contrast to the results for the low coverage regime (Paper I), the release mechanism is a function of the multilayer thickness and composition, displaying dramatically different behavior between Ar, Kr, Xe, CH_4, N_2, O_2, and CO. Two primary desorption pathways are observed. The first occurs between 100 and 150 K and manifests itself as sharp, extremely narrow desorption peaks. Temperature programmed desorption is utilized to show that these abrupt desorption bursts are due to pressure induced structural failure of the ASW overlayer. The second pathway occurs at low temperature (typically <100 K) where broad desorption peaks are observed. Desorption through this pathway is attributed to diffusion through pores formed during ASW deposition. The extent of desorption and the line shape of the low temperature desorption peak are dependent on the substrate on which the gas underlayer is deposited. Angle dependent ballistic deposition of ASW is used to vary the porosity of the overlayer and strongly supports the hypothesis that the low temperature desorption pathway is due to porosity that is templated into the ASW overlayer by the underlayer during deposition. © *2013 American Institute of Physics*. [http://dx.doi.org/10.1063/1.4793312]

I. INTRODUCTION

We investigate in detail the mechanisms for the release of trapped gases from underneath amorphous solid water (ASW) films in this (Paper II) and the preceding companion paper (Paper I).[1] The trapping and retention of volatile gases by ASW is important to understanding a wide array of astrophysical processes including the abundance of molecules in the interstellar medium[2] and the possibility that many types of gases were originally brought to earth by comets.[3–14] Early work in this area has come from Bar-Nun *et al.*[4–7] who have studied the trapping of a variety of gases by ASW including CH_4, CO, CO_2, N_2, Ne, and Ar. Others have expanded upon this early work in an effort to move toward more astrophysically relevant models.[12, 13, 15, 16] However, a detailed understanding of gas trapping and release mechanisms remain elusive.

Our original work in this area began with observation of the abrupt, episodic release of carbon tetrachloride deposited underneath an ASW film. The rapid desorption occurred in concert with a "bump" in the temperature programmed desorption (TPD) spectrum of ASW.[17] The "bump" arises as the kinetically metastable, higher free energy (vapor pressure) ASW transforms into the lower free energy, thermodynamically stable crystalline ice, resulting in a reduction in the va-

por pressure and desorption rate.[17–22] The release is due to crystallization-induced cracks which open a connected pathway to vacuum, allowing the volatile underlayer to escape in a rapid episodic desorption event dubbed the "molecular volcano."[17,23–25] In a recent paper, we exploited the "molecular volcano" desorption peak to characterize the crack formation process.[25]

In Paper I,[1] we focused on the low coverage regime where the release mechanism is controlled by crystallization-induced cracks formed in the ASW overlayer itself. For that reason, the results in that regime were largely independent of the particular gas underlayer. The "molecular volcano" desorption peak was used to show that crack formation occurs via a "top-down" mechanism in concert with crystallization. In the mechanism, crystallization begins at or near the top of the ASW film and then, after some temperature dependent induction time, a crystallization/crack front propagates into the film. Kinetic simulations based on this model were in good agreement with the experimentally observed volcano peak temperatures for a range of overlayer thicknesses and TPD heating rates.

In the present paper (Paper II), we focus on the high coverage regime where new desorption pathways become accessible prior to ASW crystallization. In contrast to the results for the low coverage regime (Paper I),[1] this release mechanism is a function of the underlayer thickness and composition, displaying dramatically different behavior between Ar,

[a] Authors to whom correspondence should be addressed. Electronic addresses: scott.smith@pnnl.gov and bruce.kay@pnnl.gov.

Kr, Xe, CH_4, N_2, O_2, and CO. Two primary desorption pathways are observed. The first typically occurs between 100 and 150 K and manifests itself as sharp, extremely narrow desorption peaks. These abrupt desorption bursts are shown to be due to pressure induced structural failure of the ASW. The second pathway occurs at low temperature (usually <100 K) where broad, smoothly varying peaks are observed. Desorption through this pathway is attributed to diffusion through pores formed during ASW deposition. The extent of desorption and the line shape of the low temperature desorption peak are dependent on the substrate on which the gas underlayer is deposited. This suggests that the surface structure of the gas underlayer affects the morphology of the ASW overlayer. Angle dependent ballistic deposition of the ASW is used to vary the porosity of the overlayer and confirm that the low temperature desorption pathway is due to porosity that is inherent in the ASW overlayer upon deposition.

II. EXPERIMENTAL

The ultra-high vacuum system (UHV) used here is exactly the same as that described in detail in Paper I.[1] For that reason, only a brief overview of the experiment will be given here. All experiments were conducted using a 1-cm diameter Pt(111) substrate spot-welded to tantalum leads in an UHV with a base pressure of $<1 \times 10^{-10}$ Torr. The sample is cooled by a closed cycle helium cryostat to a base temperature of ~25 K. Temperature was measured by a K-type thermocouple spot-welded to the back of the Pt(111) substrate and the temperature was controlled by resistive heating with a precision of better than ±0.01 K. The absolute temperature was calibrated to an accuracy of better than ±2 K. The Pt(111) surface was passivated by the deposition of a graphene layer which was formed by heating the Pt(111) substrate to 1100 K in the presence of decane.

Deposition on the graphene coated Pt(111) surface was carried out using two quasi-effusive molecular beams. The water beam was created by expanding 2 Torr of water vapor through a 1-mm diameter orifice and three stages of differential pumping. The incident water beam was slightly larger than the 1 cm diameter of the Pt(111) substrate and had a flux of 0.87 ML/s (at normal incidence). A second molecular beam was utilized to deposit Ar, Kr, Xe, CH_4, N_2, O_2, or CO by expanding 2.5 Torr of room temperature gas through a 1-mm diameter orifice and passing through four differential pumping stages before impinging on the sample at normal incidence with a diameter of 0.75 cm. The deposition rate of each gas was 0.27 (Ar), 0.25 (Kr), 0.29 (Xe), 0.57 (CH_4), 0.37 (N_2), 0.26 (O_2), and 0.33 (CO) ML/s. TPD spectra were obtained using linear heating rates and an Extrel quadrupole mass spectrometer in a line-of-sight configuration. Water desorption was monitored at m/z = 18 while individual gases were monitored at m/z = 40 (Ar), 84 (Kr), 132 (Xe), 15 (CH_4), 28 (N_2), 32 (O_2), and 28 (CO). The intensity of the mass spectrometer signal was converted into an absolute desorption rate utilizing the area under the monolayer desorption peak of H_2O on Pt(111) or the area under the monolayer desorption peak on graphene for Ar, Kr, Xe, CH_4, N_2, O_2,

or CO. Unless noted otherwise, the gas underlayer and ASW overlayer were deposited at normal incidence. In Sec. III C, the deposition angle for the ASW overlayer is varied.

III. RESULTS AND DISCUSSION

A. Pre-crystallization gas burst release

As mentioned above, Paper I[1] focused on the 1 ML coverage regime where the release mechanism was controlled by crystallization-induced cracks formed in the ASW overlayer itself. In that case, the results were largely independent of the particular gas underlayer. Here in Paper II, we focus on understanding gas release for underlayer coverages greater than one monolayer. Figure 1 displays TPD spectra for 5 ML of Ar deposited underneath a 300 ML ASW overlayer and heated at 1 K/s. The Ar spectrum (bottom trace) has three desorption peaks. The two higher temperature desorption peaks were observed in Paper I. The peak at 162.5 K labeled "volcano" is due to desorption through cracks formed in the ASW overlayer during crystallization and the peak at 178.8 K labeled "trapped" is from gas that does not desorb during the volcano peak desorption but remains trapped until the ASW itself desorbs. The peak at 130 K was not observed in the low coverage (1 ML) experiments in Paper I and occurs well below the onset of ASW crystallization (confirmed by infrared spectroscopy, not shown). While the 130 K peak is sharp and narrow like the "volcano" peak, it is distinctly different in that it is accompanied by a corresponding desorption peak in the ASW spectrum (top trace). The 130 K desorption feature accounts for the desorption of ~60% of the Ar and ~20% of the ASW overlayer. The observation of sharp pre-crystallization peaks has also been reported by Bar-Nun *et al.*[5–7] who observed the ejection of ice needles from gases covered by much thicker ASW films (~2 μm which is ~6600 ML) and attributed the effect to pressure exerted by the gas. Therefore, we propose that pressure exerted by the Ar becomes high enough to induce a catastrophic failure in the ASW barrier resulting in the ejection of some of the ASW itself. Hereafter, we refer to these sharp pre-crystallization desorption features as "burst" peaks.
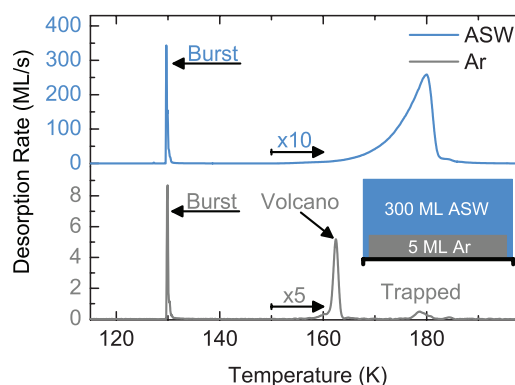
FIG. 1. TPD spectra for 5 ML of Ar (bottom trace) underneath 300 ML of ASW (upper trace) at a heating rate of 1 K/s. The Ar spectrum has three desorption features labeled "burst," "volcano," and "trapped." The Ar "burst" peak is coincident with a sharp desorption peak in the ASW spectrum which is accounts for the desorption of ~20% of the ASW overlayer.
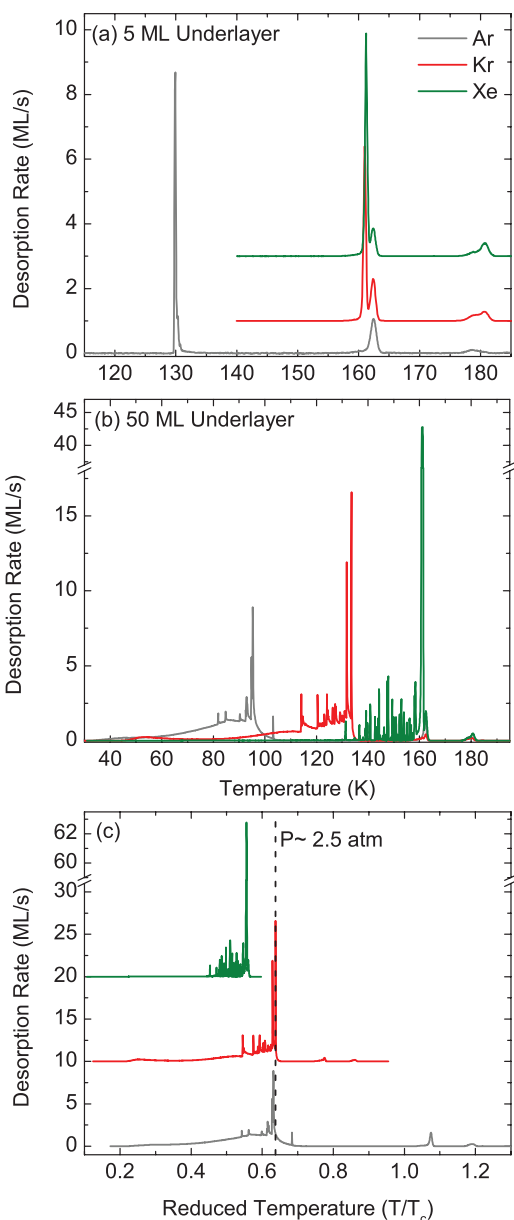
FIG. 2. TPD spectra for (a) 5 ML and (b) 50 ML of Ar (gray line), Kr (red line), and Xe (green line) beneath 300 ML ASW heated at a rate of 1 K/s. (c) The TPD spectra from (b) plotted versus the reduced temperature, T/T_c, which was obtained by dividing the temperature for each gas by its respective T_c (150.87 K for Ar, 209.41 K for Kr, and 289.77 K for Xe). Rescaling aligns the most prominent peaks for Ar and Kr to the same reduced temperature (vertical dashed line) corresponding to a pressure of ~2.5 atm.

The exact temperature and number of the burst desorption peaks is dependent on the particular gas and the thickness of the underlayer. Figure 2(a) displays the TPD spectra for 5 ML of Ar, Kr, and Xe deposited underneath 300 ML of ASW heated at 1 K/s. A burst peak at 130 K is observed only for Ar while Kr and Xe have sharp desorption peaks at temperatures just below the molecular volcano peak. Increasing the thickness of the underlayer produces dramatic changes in the TPD spectra. This is illustrated in Figure 2(b) where the TPD spectra for 50 ML of Ar, Kr, and Xe deposited underneath 300 ML of ASW heated at 1 K/s are displayed. Comparing Fig. 2(a) to Fig. 2(b), the largest Kr desorption peaks have

shifted to temperatures far lower than the molecular volcano peak while the sharpest Xe peak remains near the molecular volcano peak (just as in Fig. 2(a)). For all of the gases, there are multiple sharp burst peaks that occur over a range of temperatures. These sharp peaks reproducibly occur in the same temperature region but their exact temperature and intensity varies between experiments. Their stochastic nature is evidence for pressure-induced failure of the inhomogeneous structure of the ASW overlayer.

One explanation for the gas dependent TPD results is the difference in vapor pressures. For example, at 60 K the vapor pressure of Ar is 6.2 Torr, Kr is 1.1×10^{-2} Torr and Xe is 5.5×10^{-4} Torr. This means that at a given temperature Ar exerts much more pressure on ASW than Kr or Xe, and as a result, the Ar burst peaks occur at a lower temperature than for Kr and Xe. This argues that the burst peaks are not dependent on the nature of the particular gas specie per se, but instead only on the gas pressure.

Confirmation that the burst peak desorption is pressure-induced can be obtained by rescaling the TPD spectra of Ar, Kr, and Xe by their respective critical temperatures, T_c. The theory of corresponding states says that liquid properties, such as the vapor pressure, can be rescaled onto a common curve.[26, 27] Figure 2(c) displays the spectra from Fig. 2(b) plotted versus the reduced temperature which was obtained by dividing the temperature for each gas by its respective T_c (150.87 K for Ar, 209.41 K for Kr, and 289.77 K for Xe). Rescaling aligns the pre-volcano sets of Ar and Kr desorption peaks to the same temperature range. The reduced temperature for the most prominent Ar and Kr peaks (denoted by the vertical dashed line) corresponds to a pressure of ~2.5 atm. The Xe peak does not align with the Ar and Kr but instead is shifted to a lower reduced temperature. Because the Xe burst peak is so close to the volcano peak, the Xe may desorb when the ASW weakens just prior to crystallization and before reaching the temperature needed to get a pressure of 2.5 atm. This release just before the volcano is observed for thinner layers of Kr and Xe in Fig. 2(a). Together, the similarity between the reduced temperature desorption patterns of Ar and Kr and the ejection of ASW (Fig. 1) indicate that the sharp pre-crystallization desorption peaks are pressure-induced. Note, that later in this work we conclude that very small changes in the underlayer can lead to morphology differences in the ASW. Therefore, ASW will have different mechanical properties depending on what it is deposited upon which is the ultimate driver of differences, for example, between Figs. 2(a) and 2(b).

The appearance of burst peaks leads to an increase in the total amount of gas that desorbs prior to the volcano peak. In Paper I, the "trapped" fraction (the fraction of the gas that desorbs in the "trapped" peak) as a function of ASW overlayer thickness was used to characterize the vertical crack length distribution. The dependence of the trapped fraction on the underlayer thickness beneath a fixed amount of ASW will now be considered. Figure 3 displays the trapped fraction of Ar, Kr, and Xe versus the underlayer coverage for a fixed 300 ML ASW overlayer. At very low (submonolayer) underlayer coverages the trapped fraction is high. This is because when cracks propagate from the outer surface there
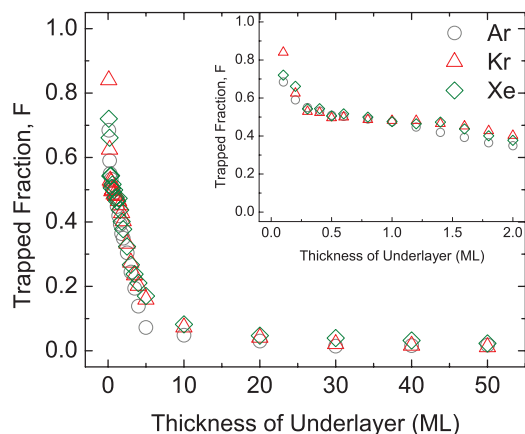
FIG. 3. The trapped fraction of Ar (○), Kr (△) and Xe (◇) versus underlayer thickness for a fixed 300 ML ASW overlayer. (Inset) An expanded view of the same data from 0 to 2 ML which shows that between 0.5 and 1.5 ML the trapped fraction is relatively insensitive to the underlayer thickness.

is a high probability of reaching an area on the substrate where there is no underlayer gas, much like drilling a "dry well." This dependence on coverage is evidence for a lack of mobility in the underlayer meaning that a single crack is insufficient to desorb the entire underlayer. Note that from 0.5 to 1.5 ML (inset), the trapped fraction is relatively insensitive to the underlayer thickness meaning that the underlayer is spread across the substrate, i.e., there are no "dry" wells. This coverage range was explored in Paper I and the inset data support the idea that the changes in trapped fraction with overlayer coverage are due to the crack length distribution and not "dry" wells. Also note that in this coverage range there is very little to no pre-crystallization desorption.

Above ∼1.5 ML the trapped fraction drops monotonically, mostly due to larger fractions of the underlayer desorbing before the molecular volcano peak (i.e., before the onset of crystallization). This is consistent with the large amount of pre-volcano desorption observed for 50 ML of Ar, Kr, or Xe

compared to 5 ML (Fig. 2(b) versus Fig. 2(a)). Interestingly, at the temperatures where the burst peaks are observed, all of the gases are below their respective critical point so increasing the amount in the underlayer should not increase the pressure and consequently the amount of pre-crystallization "burst" peak gas desorption. Above underlayer thicknesses of ∼5 ML the trapped fraction is relatively constant which suggests that the distribution of desorption pathways becomes independent of the underlayer thickness.

In Sec. III B, we investigate another pre-crystallization desorption pathway that is more directly dependent on the ASW overlayer structure and helps to explain the seemingly anomalous dependence on the underlayer thickness.

B. Low temperature "diffusive-like" release

In Sec. III A, we observed that placing multilayers of Ar, Kr, or Xe beneath ASW can lead to desorption at temperatures below the crystallization-induced molecular volcano. Catastrophic desorption events, "bursts," which cause the coincident desorption of ASW along with the underlayer, were shown to arise from high pressures generated by the underlayer leading to structural failure of the ASW. However, the dependence of pre-volcano desorption on the underlayer thickness remains something of a mystery. Thinking in terms of an ideal gas, this should be easy to explain since more molecules in a space should increase the pressure. However, each gas is below its respective critical point. Therefore, the pressure exerted by the underlayer on the ASW should be independent of underlayer thickness. Here, we investigate further the effect of the underlayer thickness and the nature of the gas species on the pre-crystallization release of trapped gases.

The effect of underlayer thickness for Ar, Kr, Xe, CH₄, N₂, O₂, and CO is shown in Fig. 4. Displayed in separate panels are the TPD spectra for each gas for a series of underlayer thicknesses from 1 to 50 ML beneath 300 ML of
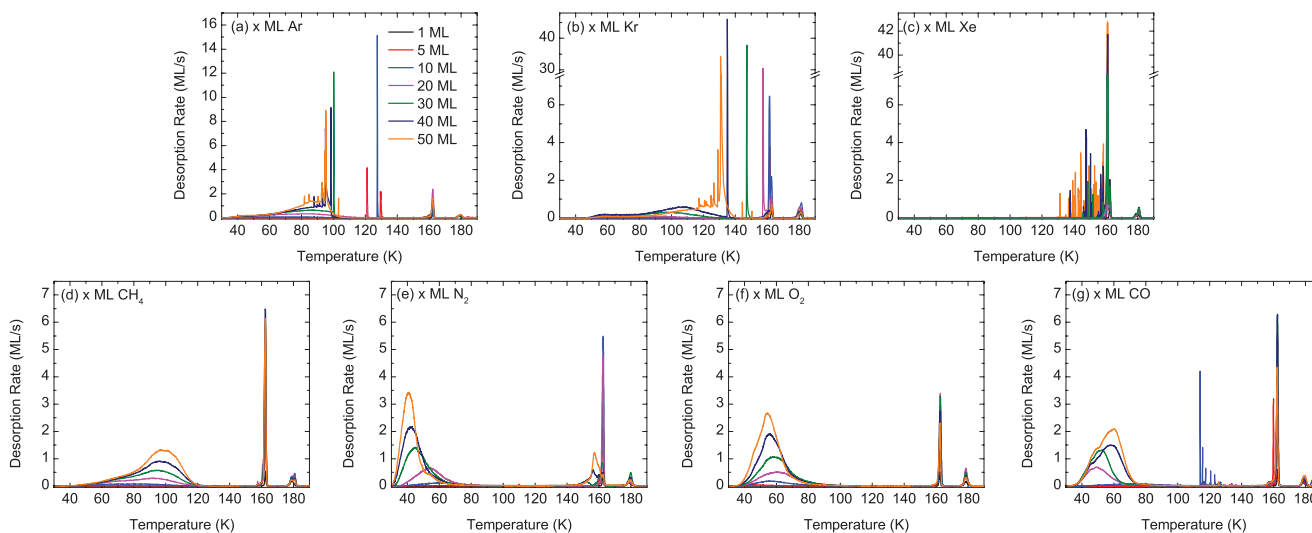

FIG. 4. TPD spectra (a) Ar, (b) Kr, (c) Xe, (d) CH₄, (e) N₂, (f) O₂ and (g) CO for underlayer thicknesses of 1, 5, 10, 20, 30, 40 and 50 ML and a 300 ML ASW overlayer. The heating rate was 1 K/s. The spectra for atomic underlayers display primarily narrow burst peaks that increase in number and intensity with underlayer thickness. The molecular species have a single broad low temperature desorption feature that shifts to low temperature with underlayer thickness.
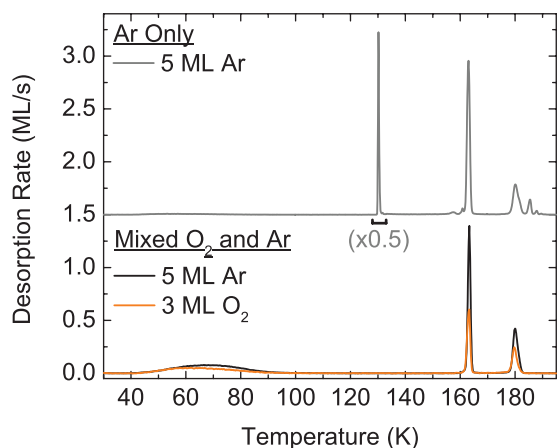
FIG. 5. Comparison of two TPD experiments performed at a heating rate of $\beta = 1$ K/s. The upper trace is offset by 1.5 ML/s and the peak at 130 K has been multiplied by 0.5. The upper spectrum is for 5 ML of Ar is deposited on graphene and covered by 340 ML of ASW. This spectrum displays a characteristic "burst" peak at 130 K. The lower spectra are from an experiment where 5 ML of Ar is co-dosed with 3 ML of O_2 and covered by 340 ML of ASW. In these spectra no "burst" peak is observed, but rather both O_2 and Ar desorb in a broad low temperature feature centered around 68 K.

ASW. There are clear differences in desorption behavior between the gases. For example, the spectra for Ar, Kr, and Xe (Figs. 4(a)–4(c)) are dominated by the sharp burst peaks discussed in Sec. III A, while in the spectra for CH_4, N_2, and O_2 (Figs. 4(d)–4(f)) these peaks are missing. Instead these gases, along with CO (Fig. 4(g)), have a broad low temperature desorption feature that increases with underlayer coverage. A hint of this broad desorption feature is also apparent in the Ar and Kr spectra. The species dependence of the pre-crystallization desorption features (both the burst and the broad low temperature peaks) is very different from the results in Paper I for 1 ML thick underlayers. In that work, the temperature of the molecular volcano and trapped fraction peaks were found to be independent of the species comprising the underlayer. In contrast, the results in Fig. 4 clearly illustrate that multilayer desorption changes with the desorbing species.

A possible explanation for the species dependence observed in Fig. 4 is the relative size of the atoms and molecules. For example, it is possible that a small amount of porosity inherent in the ASW overlayer allows a molecule like O_2 (comprised of atoms of a second row element) to escape because its diameter perpendicular to the bonding axis is smaller than that of the monatomic gases (Ar, Kr, and Xe which are third row and above elements). To test this hypothesis, experiments where the underlayer was comprised of a mixture of Ar and O_2 were conducted. Figure 5 compares the TPD spectra from a neat Ar underlayer with that of an Ar/O_2 mixture underneath 340 ML of ASW heated at 1 K/s. The spectrum (upper trace) for 5 ML of Ar is similar to the results in Fig. 1 displaying a burst peak at ∼130 K. The spectrum for the mixture, comprised of 5 ML of Ar and 3 ML of O_2 (lower trace), is clearly missing burst peaks for both Ar and O_2. Thus, a simple size argument alone cannot account for the observations in Fig. 4. Instead it appears that the presence of O_2 in the underlayer has facilitated the low temperature desorption of Ar, causing it to desorb before enough pressure is built up to induce fail-

ure in the ASW overlayer. In Sec. III C, we further explore the effects of the underlayer on the ASW overlayer morphology.

Given the results of Figs. 4 and 5, the sharp pre-volcano peaks (as shown in Sec. III A) are still attributed to pressure-induced desorption. However, the broad low temperature desorption appears to arise from a different mechanism. Vapor pressures in this low temperature range are much lower and the broad peaks are not accompanied by the desorption of water. Instead, the Gaussian-like shapes are suggestive of a diffusive process.

The mechanism of the broad low temperature desorption peak was investigated using the desorption of a fixed amount of O_2 as a function of the ASW overlayer thickness. Figure 6(a) displays the TPD spectra of 50 ML of O_2 placed beneath increasing amounts of ASW at a ramp rate of 1 K/s. For ASW thicknesses from 50 to 300 ML, the peak shifts to higher temperature and broadens with increasing thickness, which is qualitatively consistent with a diffusive process. Above 300 ML, the peak temperatures do not shift to higher temperature with increasing thickness but instead pile up at 58 K.

In previous work, we investigated the permeation of gases through supercooled liquids, and while not exactly the same physical process as here, the mathematics for diffusion are equivalent.[28,29] In that work, we showed that diffusivity through an overlayer could be obtained using the following relationship:

$$D(T_{Peak}) = \frac{\alpha \beta L^2}{T_{Peak}^2}\left(\frac{E}{R}\right), \tag{1}$$

where L is the overlayer thickness, β is the heating rate, and T_{Peak} is the temperature at the desorption peak. The activation energy is E, the gas constant is R, and α is a scale factor that depends on the specific point on the desorption curve used in the analysis ($\alpha = 0.415$ for the desorption peak). In Eq. (1), the diffusivity is given by the quantity $\beta L^2/T^2_{Peak}$, to within a constant factor of $\alpha E/R$. Figure 6(b) is an Arrhenius plot of the quantity $\beta L^2/T^2_{Peak}$ using the low temperature O_2 desorption peak from a series of experiments with heating rates from 0.1 to 2 K/s and overlayer thicknesses from 50 to 2000 ML. At low temperatures all of the data points lie reasonably close to a line but deviate sharply from that line at higher temperatures ($T > \sim 50$ K). This deviation is due to the "piling up" of the low temperature peak at overlayer thicknesses above ∼300 ML as is seen in Fig. 6(a) and also in the desorption spectra for the other heating rates (not shown).

If the low temperature peaks were due to diffusion, then the data from the various ramp rate experiments should collapse onto a common straight line (Fig. 6(b)). This is not the case over the entire thickness range. The points are close together at low temperatures/coverage but diverge vertically from the line at higher temperatures. A fit to the $\beta = 1$ K/s data set for ASW thicknesses up to 300 ML is given by the solid line in Fig. 6(b). Conversion of this fit line to diffusivity using Eq. (1) and the procedure described previously,[28,29] yields Arrhenius diffusion parameters of $\nu = 2.5 \times 10^{-8}$ cm^2/s and $E = 3.7$ kJ/mol. These parameters were used to simulate the 1 K/s O_2 low temperature desorption spectra in
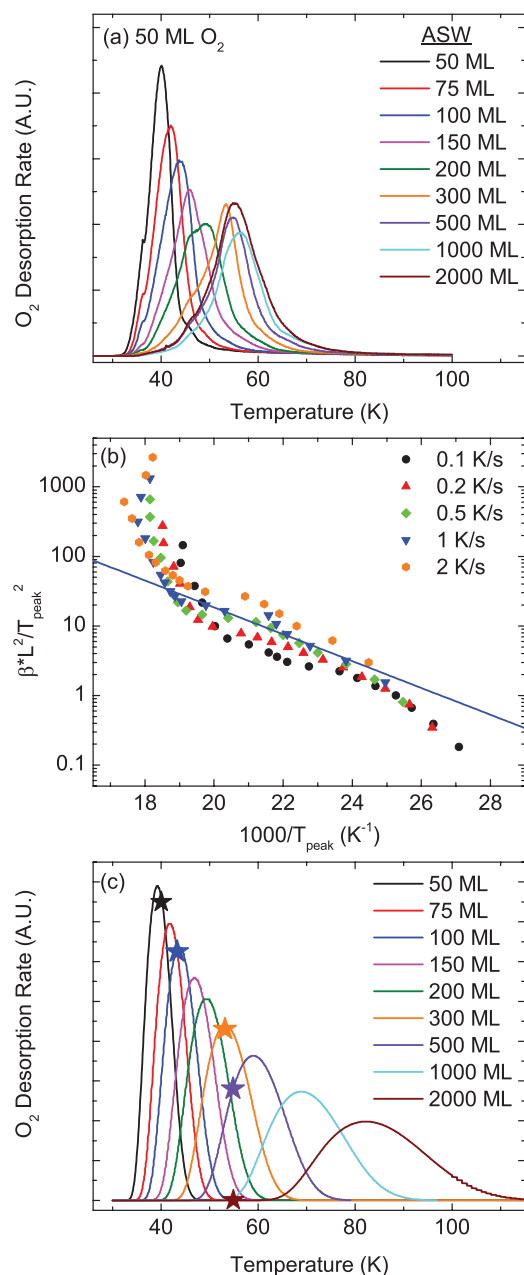
FIG. 6. (a) Plot of the low temperature region of a series of TPD spectra for 50 ML O_2 beneath thicknesses of ASW from 50 to 2000 ML. The heating rate was 1 K/s. (b) Arrhenius plot of the quantity, $\beta L^2/T^2_{Peak}$ (symbols), where β is the heating, L is the ASW overlayer thickness, and T_{Peak} is the peak temperature of the low temperature desorption feature for the TPD spectra in (a) (1 K/s) and analogous sets of TPD spectra with heating rates of 0.1, 0.2, 0.5, and 2 K/s. The quantity $\beta L^2/T^2_{Peak}$ is proportional to the diffusivity of the gas through the overlayer (see Eq. (1) in the text). A fit to the β = 1 K/s data set for ASW thicknesses up to 300 ML is given by the solid line and yields Arrhenius diffusion parameters of $\nu = 2.5 \times 10^{-8}$ cm^2/s and E = 3.7 kJ/mol. (c) Simulated TPD spectra at β = 1 K/s assuming a diffusion model for a variety of overlayer thicknesses using the Arrhenius parameters obtained in (b). The "stars" demark the experimental peak temperatures for the corresponding overlayer thicknesses from (a).

FIG. 7. (a) Plot of the desorption peak temperature versus ASW overlayer thickness for 50 ML of CO, O_2, N_2 and CH_4 on graphene and heated at a rate of 1 K/s. The dashed lines are diffusion model predictions using parameters fit to the overlayer data up to 300 ML for each gas. (b) Plot of the desorption peak temperature data in (a) rescaled by the critical temperature, T_{Peak}/T_c. The horizontal dashed lines demark values of T_{Peak}/T_c where the CO and CH_4 data and the O_2 and N_2 data appear to converge at large ASW overlayer thicknesses. These reduced temperatures correspond to pressures of 0.4 and 0.004 atm.

Fig. 6(a) using a one-dimensional diffusion model described previously.[28–30] The simulation results are displayed in Fig. 6(c). There is good qualitative agreement between the experimental (Fig. 6(a)) and simulated (Fig. 6(c)) spectra, in that the peaks shift to higher temperature and broaden, for
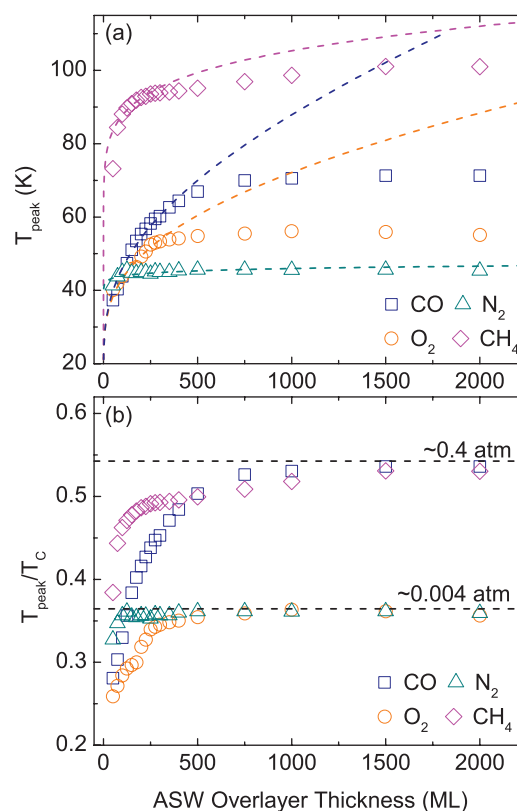
ASW thicknesses up to 300 ML. The stars in Fig. 6(c) demark the experimental desorption peak temperatures which are in good agreement with the simulations for 50, 100, and 300 ML thick ASW overlayers. However, the agreement is worse for thicker overlayers with the 500 ML being slightly off and 2000 ML simulation being more than 25 K different than the experiment. These results suggest that for O_2 at low temperature and at thicknesses below 300 ML, the release mechanism appears to be diffusive, but at higher temperatures and above 300 ML, the diffusive mechanism breaks down.

The analogous experiments with 50 ML thick underlayers and varying ASW thicknesses were preformed for CO, N_2, and CH_4, which have similar low temperature desorption behavior as O_2 (see Fig. 4). Figure 7(a) is a plot of the low temperature desorption peak temperatures (symbols) versus ASW overlayer thickness for CO, N_2, CH_4, and O_2. The gases all have the same behavior with the peak temperature increasing with overlayer thickness up to ∼300 ML, and above that thickness, the peak temperature remains relatively constant. The dashed lines are calculated using the diffusivities obtained from the peak temperatures below 300 ML for each individual gas using Eq. (1) and the procedures described above. It is clear that the experimental peak temperatures

(symbols) deviate from the diffusion prediction (dashed line) at overlayer thicknesses above 300 ML.

The appearance of a fixed desorption peak temperature for thicker overlayers is reminiscent of the "burst" peak desorption mechanism discussed in Sec. III A. To test the idea that the breakdown of the diffusion model was due to an increase in pressure, the temperature axis was rescaled by the critical temperature. The rescaled data are plotted in Fig. 7(b) and the points for the various gases do not collapse onto a single common curve. There appears to be a convergence of the CO/CH_4 and the O_2/N_2 data at large overlayer thicknesses but this is likely coincidental as it was not consistently observed for data sets with different underlayer thicknesses (data not shown). The asymptotes correspond to very low pressures of 0.4 and 0.004 atm, which are far lower than the 2.5 atm that leads to the pressure induced desorption events shown in Fig. 2. The peak temperatures for the gases in Fig. 7(a) are consistent with trapping efficiencies ($CH_4 > CO > N_2$) found by Bar-Nun *et al.*[7] and more recently by Yokochi *et al.*[16] However, preliminary studies of the binding energy of these gases on ASW or graphene do not provide a means of rescaling the data in Fig. 7(a) onto a common curve (data not shown). Thus, we do not believe that differences in binding energy satisfactorily explain the very different desorption temperatures observed here. Determination of coverage dependent binding energies on graphene and ASW will be the subject of a future publication.

The results in Figs. 6 and 7 appear to be consistent with a diffusive mechanism for thicknesses <300 ML, but the diffusive behavior breaks down for thicker overlayers. Also, if the observed phenomena were simply due to diffusion (even below 300 ML), the results should be independent of the gas itself or scalable by some physical property of the gas (e.g., vapor pressure, binding energy). This is because gas transport should be controlled by the same pore structure and connected pathways in the ASW overlayer. Thus, all of the gases including Ar, Kr, or Xe should have broad low temperature peaks similar to CO, N_2, O_2, and CH_4. As seen in Fig. 4, the low temperature desorption behavior is clearly dependent on the particular underlayer species. The expectation that diffusion be independent of the particular underlayer, assumes that the ASW morphology is independent of the underlayer. In Sec. III C, we investigate how the underlayer affects the morphology of the ASW overlayer.

C. Effect of the substrate on low temperature gas release

The results in Sec. III B show that the low temperature desorption peak is dependent on both the particular underlayer species and the amount. These differences cannot be explained by differences in the physical properties of the underlayer, e.g., vapor pressure, critical temperature, binding energy, etc. Here, we explore whether the morphology of the ASW overlayer depends on the particular gas underlayer and the substrate underneath the underlayer.

Figure 8 displays the TPD spectra for 1, 20, and 50 ML of Ar and O_2 deposited on two different substrates, namely, graphene and 2 ML of ASW on top of graphene. The Ar and
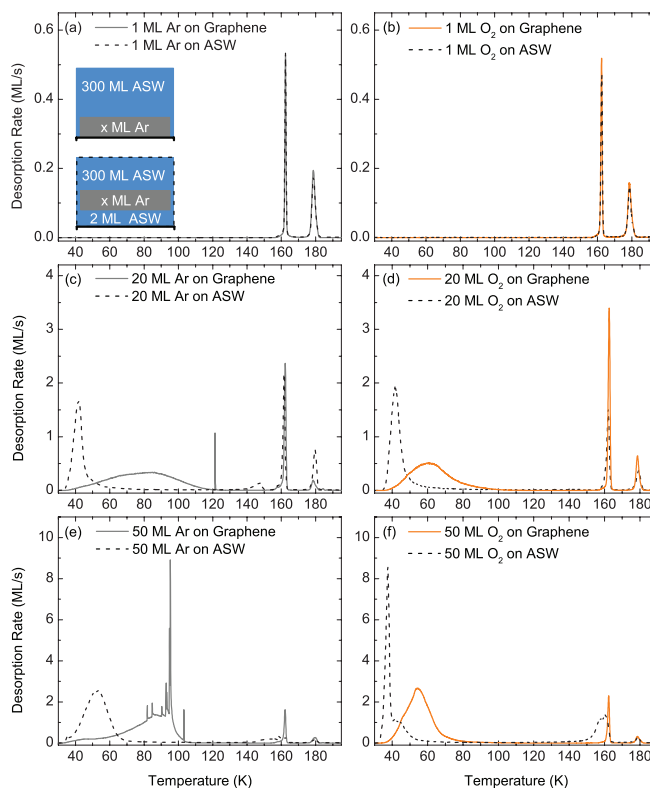

FIG. 8. TPD spectra for 1, 20, and 50 ML of Ar ((a), (c), and (e), respectively) and O_2 ((b), (d), and (f), respectively) deposited on graphene (solid lines) and 2 ML of ASW on top of graphene (dashed lines), and covered by 300 ML of ASW. The heating rate was 1 K/s. The TPD spectra for both gases are dependent on the underlying substrate.

O_2 layers were covered by 300 ML of ASW in all spectra. These gases were chosen to represent the species in Fig. 4 that have a pronounced low temperature desorption feature (O_2) and those that do not (Ar). The 1 ML thick underlayer spectra are displayed in the top row of Fig. 8. The spectra for underlayers deposited on graphene (solid lines) and on 2 ML of ASW (dashed lines) are nearly identical for both Ar (Fig. 8(a)) and O_2 (Fig. 8(b)). Both the Ar and O_2 spectra have volcano and trapped desorption peaks that occur at the same temperatures for both gases. Neither gas displays low temperature desorption peaks. These results are consistent with Paper I which showed that desorption behavior was independent of the particular gas species for 1 ML underlayers. The results here show that for 1 ML thick underlayers the underlying substrate does not have an effect on the desorption spectra. In the supplementary material (Figure S1),[31] we show that the onset of the low temperature desorption begins for both Ar and O_2 at underlayers >2 ML. In the supplementary material (Figure S2),[31] we also show that the crystallization induced crack length distribution is independent of whether the underlayer is deposited on graphene or 2 ML ASW.

In contrast to the 1 ML results, the spectra for 20 ML underlayers on the two substrates are dramatically different. The 20 ML thick underlayer spectra for Ar and O_2 are displayed in Figs. 8(c) and 8(d), respectively. On graphene (solid line), the Ar desorption is very broad and centered around 80 K, while on ASW (dashed line) the desorption is relatively narrow and shifted to 42 K. Similar results are seen for O_2 as the broad
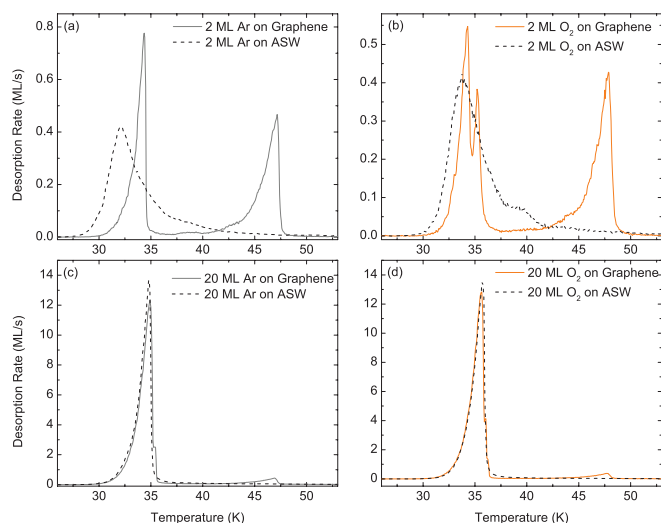
FIG. 9. Desorption of (a) 2 ML Ar, (b) 2 ML O_2, (c) 20 ML Ar and (d) 20 ML of O_2 from graphene (solid) or ASW (dashed) deposited without an ASW overlayer. The heating rate was 1 K/s. Very different desorption behavior is observed for thin Ar and O_2 layers on graphene versus ASW while the multilayer desorption temperature is substrate independent.

peak at 60 K on graphene narrows considerably and shifts to 43 K on ASW. This trend persists for 50 ML underlayers, where for Ar, a broad peak near 90 K that is punctuated by several sharp pressure-induced burst peaks on graphene, becomes a broad low temperature peak at 53 K without any burst peaks. Similarly, while the 50 ML O_2 spectrum does not exhibit sharp burst peaks on graphene, the O_2 desorption peak narrows sharply and shifts to lower temperature when deposited on 2 ML of ASW. The lower desorption peak temperature on 2 ML of ASW compared to graphene appears to be a general phenomenon. The desorption peak temperatures for 50 ML of O_2, N_2, CH_4, or CO deposited on graphene and 2 ML of ASW as a function of ASW overlayer thickness from 50 to 2000 ML are given in the supplementary material (Figure S3).[31]

The observation that the underlying substrate affects the low temperature desorption behavior opens an entirely new set of possibilities concerning the origin of low temperature desorption features. One possibility is that the substrate affects the structure of the underlayer gas and consequently the desorption behavior. Figure 9 displays the TPD spectra for Ar and O_2 from graphene and 2 ML of ASW without an ASW overlayer. The desorption spectra for 2 ML of Ar and O_2 are displayed in Figs. 9(a) and 9(b), respectively. The desorption spectra from the graphene substrate (solid lines) for both gases exhibit zero-order behavior with distinct monolayer peaks at 47 K for Ar and 48 K for O_2 and second layer desorption peaks at 34 K for Ar and at 34 K and 35 K for O_2. The monolayer peaks arise from gas desorbing from the graphene substrate and the second layer desorption peaks arise from gas desorbing from the monolayer. Despite the double peak structure for O_2, we believe that these peaks arise from desorption from the second layer and not crystallization because the TPD spectra as a function of coverage show that the two peaks fill in concert (see Figure S4 of the supplementary material).[31]

The 2 ML desorption spectra from the ASW substrate (dashed lines) are much different than those from graphene for both Ar and O_2. Neither spectrum has distinct monolayer and second layer peaks but instead both have a single broad peak with a non-zero order line shape. The leading edges of the desorption peaks on ASW are shifted to lower temperatures than the second layer desorption peaks on graphene. One possibility for this temperature shift is that on graphene the gas layer may have crystallized to a more stable structure resulting in a lower desorption rate.[19, 21, 22] However, our estimates using the enthalpies of vaporization and sublimation predict less than a degree temperature shift between the vapor pressure for the crystalline and amorphous phases of both gases. Thus, crystallization does not explain the desorption temperature differences between the two substrates.

The effect of the underlying substrate is negligible when the Ar or O_2 thickness is increased to 20 ML. The desorption spectra on graphene and ASW for both Ar (Fig. 9(c)) and O_2 (Fig. 9(d)) display zero-order desorption behavior and are nearly indistinguishable except for the small monolayer peak observed in the spectra on graphene.

The results in Fig. 9 show that the substrate does affect the underlayer structure. Graphene provides a smooth surface for layer-by-layer growth of an ordered film while the ASW substrate has a distribution of binding sites. However, the substrate effects that are readily apparent for thin underlayers (2 ML), appear to diminish as the underlayer thickness increases (20 ML). If the underlying substrate does not affect the desorption behavior for thicker multilayers, how can we explain the vastly different behavior observed in Fig. 8? One possibility is that small differences in the underlayer species change the morphology of the ASW overlayer which results in the observed substrate dependent low temperature desorption behavior.

The morphology of the ASW overlayer was varied by changing the incident deposition angle to investigate its effect on the low temperature desorption behavior. The porosity and morphology of vapor deposited ASW films can be controlled by varying the incident deposition angle.[32–39] Deposition at normal incidence results in dense, non-porous films, whereas deposition at large incident angles results in highly porous materials. The effect is based on a ballistic deposition mechanism in which incident molecules "hit-and-stick" where they land. At large incident angles random height differences during the initial film growth can block incoming flux, essentially casting shadows that result in void regions (porosity). This deposition mechanism is very robust and highly porous films for a range of materials can be grown.[40–43]

Figure 10 displays a series of TPD spectra for 50 ML of Ar underneath 500 ML of ASW deposited on graphene and heated at 1 K/s. The ASW overlayer was deposited at incident angles of 0° (top panel), 5°, 10°, 15°, and 20° (bottom panel). At normal incidence the Ar spectrum displays a series of sharp burst peaks between 70 and 90 K and a trapped desorption peak near 180 K but no broad low temperature desorption peak. As was observed in Paper I, there is no volcano peak for this thickness of an ASW overlayer. The 5° and 10° spectra show that the number and magnitude of burst peaks decreases with increasing deposition angle. In the 15°
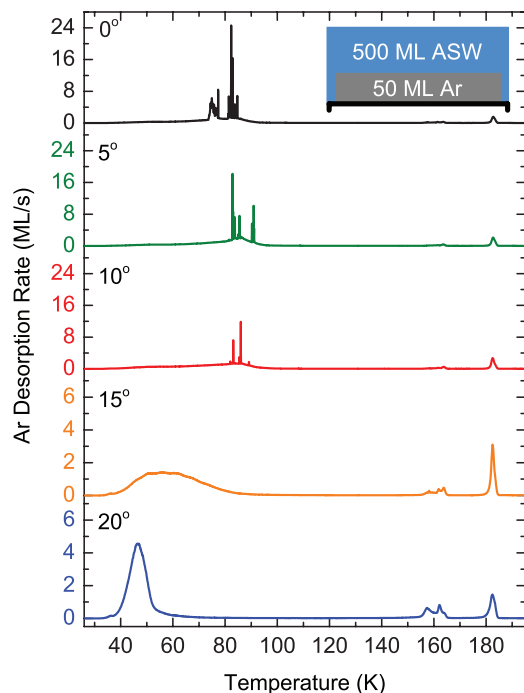
FIG. 10. TPD spectra of 50 ML Ar deposited on graphene with 500 ML ASW deposited above the Ar layer at incident deposition angles of 0° (top), 5°, 10°, 15° and 20° (bottom). The Y-axis scale for the first three spectra is identical to emphasize the decrease in magnitude of the sharp desorption features with ASW deposition angle.
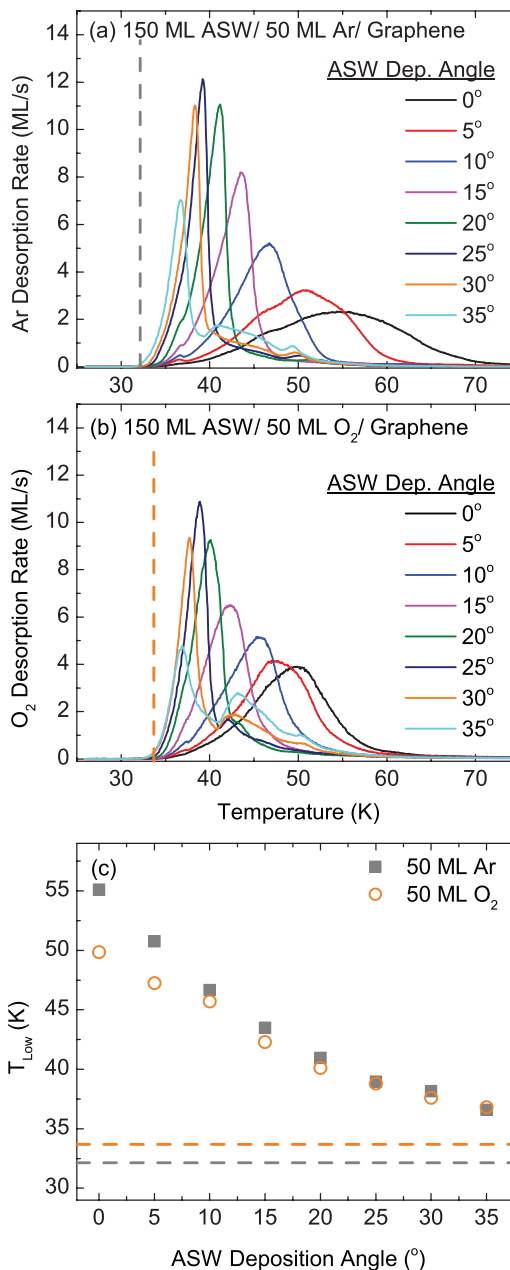

FIG. 11. Desorption of 50 ML of (a) Ar and (b) O_2 from graphene after being covered by 150 ML of ASW deposited at various angles of incidence. The low temperature desorption peak for 50 ML of the respective gases from graphene is marked by a vertical dashed line. (c) Comparison of the low temperature peaks in (a) and (b) for Ar (squares) and O_2 (circles).

spectrum, the burst peaks have completely disappeared and instead a broad low temperature desorption peak emerges. At a deposition angle of 20° the low temperature peak sharpens and shifts to even lower temperature. This temperature shift is reminiscent of that observed in Fig. 8 where the low temperature peaks for multilayers of Ar and O_2 on graphene shifted to lower temperature and sharpened on ASW. This correlation strongly suggests that ASW overlayers grown on underlayers deposited on an ASW substrate are more porous than those grown on a graphene substrate. The main point of Fig. 10 is that changes in the ASW overlayer morphology can reproduce the entire range of observed low temperature desorption behaviors; from no low temperature peak for nonporous films (0° deposition) to a pronounced low temperature peak for more porous overlayers (20° deposition).

It is surprising that such a small off-normal angle is able to produce such a dramatic effect. Typically, the development of measurable porosity does not begin until deposition angles of 35° or above.[32–35, 39] This is demonstrated for 1 ML of O_2 on graphene and 2 ML of ASW in Figure S5 of the supplementary material.[31] Clearly, the surface of 50 ML of Ar induces more porosity in the ASW overlayer than does the surface of 1 ML of Ar. One possibility is that the thick Ar layer has enough roughness to act as a template that enhances the effect of the deposition angle.

The ability of off-normal deposition of the ASW overlayer to reproduce the observed low temperature behavior is further illustrated in Fig. 11. The TPD spectra for 50 ML of Ar and O_2 deposited on a graphene substrate and covered by 150 ML of ASW where the incident ASW deposition angle was varied from 0° to 35° in 5° increments are displayed in Figs. 11(a) and 11(b), respectively. The spectra for both gases show that the low temperature desorption peak shifts to lower temperature with increasing deposition angle. The peaks begin to "pile-up" as the porosity (pore size) increases. The vertical dashed lines mark the desorption peak temperatures for 50 ML of the uncovered gases on graphene. Above 35°, significant unfettered desorption occurs which is consistent with the formation of relatively large pores at these higher deposition angles (not shown). Figure 11(c) is a plot of the desorption peak temperature as a function of deposition angle for both gases. The O_2 peak temperature (open

circles) is lower than that of Ar (solid squares) until a deposition angle of 10°. Above 10°, the desorption peaks for the two gases are about the same. This difference in desorption temperature below 10°, is likely due to differences in the surface structure or properties (rigidity) of the two underlayers. The results in Fig. 11 show a direct connection between incident deposition angle (porosity) and the temperature and shape of the low temperature desorption feature. These results further support the hypothesis that the ASW overlayer morphology is responsible for the observed low temperature desorption behavior dependence and its apparent dependence on the particular underlayer species.

IV. CONCLUSIONS

In this (Paper II) and the preceding companion (Paper I) paper, the mechanisms for the release of trapped gases from underneath ASW films were investigated. Here (Paper II), the focus was on the high coverage regime where new desorption pathways become accessible prior to ASW crystallization, i.e., pre-volcano release. We observed two distinct pre-crystallization desorption pathways. The first pathway is illustrated in Fig. 1 where sharp, narrow gas desorption peaks are observed to occur in concert with abrupt ASW desorption peaks. These extremely narrow desorption peaks were termed "burst" peaks and the spectra in Fig. 2 show that their number, intensity, and temperature range are dependent on the particular underlayer species. However, rescaling the temperature by the critical temperature, T/T_c, causes the most prominent desorption peak for the gases to occur at the same reduced temperature. These results confirm that the burst peaks are due to pressure-induced failure of the ASW overlayer.

While the differences in the pre-crystallization desorption behavior of Ar, Kr, and Xe could be reconciled by accounting for the gas pressure, the spectra in Fig. 4 showed that this was not the case for all gases. In particular, the spectra for CH_4, N_2, O_2, and CO show no burst peaks but instead have a broad low temperature peak that increases with the underlayer thickness. The peak line shape is reminiscent of gas diffusion through an overlayer. The low temperature peak as a function of overlayer thickness was modeled as a diffusive process in Figs. 6 and 7. For overlayer coverages below 300 ML, the desorption peak temperature was consistent with gas diffusion through an overlayer, however, above 300 ML the diffusive behavior broke down. In addition, several other observations including the peak temperature dependence on the particular gas and gas thickness, were inconsistent with the gas diffusion through an overlayer with the same morphology for each species. The observed "diffusive" behavior is consistent with "Knudsen-like" transport (a combination of surface diffusion and desorption/re-adsorption transport) through pores created in the ASW overlayer during deposition on the particular gas underlayer. A plausible explanation for the observed "piling-up" desorption peak behavior in Figs. 6 and 7 is discussed further below.

Dramatic differences in the low temperature desorption behavior were observed when the underlayer was deposited on a relatively smooth graphene substrate versus an ASW layer containing a wide distribution of binding sites (Fig. 8). For a given gas species, the desorption peak temperature was consistently lower on ASW than on graphene, even for 50 ML thick underlayers. The substrate effects could not be attributed to differences in the phase of the underlayer (crystallization) and the results in Fig. 9 showed that for thicker films the substrate had only a negligible effect on the desorption behavior of an uncovered underlayer. These results led us to look into how the morphology of the ASW overlayer itself affects the low temperature desorption behavior. Deposition at off-normal angles was used to vary the porosity of the ASW overlayer. The results in Figs. 10 and 11 support the hypothesis that low temperature desorption behavior is directly related to the morphology (porosity) of the ASW overlayer.

The correlation of the ASW morphology with the low temperature desorption behavior explains the apparently anomalous low temperature desorption behavior. For example, the species dependent behavior observed in Fig. 4 where CH_4, N_2, O_2, and CO had broad low temperature desorption peaks and Ar, Kr, and Xe did not, could be the result of differences in the surface roughness between the two groups. It is plausible that the atomic gases form a smoother outer surface for the ASW deposition than the molecular gases. Surface morphology could lead to an increase in the porosity of the ASW overlayer in a similar way as glancing angle deposition does, i.e., by providing areas where the incoming flux is shadowed even when the deposition is at normal incidence. As observed in Fig. 8, the morphology of the substrate (inhomogeneous ASW versus smooth graphene) can have a dramatic effect on the low temperature desorption behavior and these effects persist in underlayers at least as thick as 50 ML. The differences in surface morphology need not be much to have an effect on the low temperature desorption behavior. For example, in Fig. 10 large effects for incident deposition angles less than 20° and as low as 5° were observed, where in previous work deposition at these angles results in only negligible changes in the ASW film porosity and density.[35,39] Thus, it appears that relatively small changes in the ASW overlayer morphology (density, pore structure) can arise from templating effects from the gas layer on which ASW is deposited.

Two other observations can be explained by the idea that a particular underlayer species affects the morphology of the ASW overlayer. The lack of burst peaks for molecular underlayers (Fig. 4) could be the result of the pressure relief provided by the low temperature desorption pathway. In other words, the pressure needed to create the burst peaks for these gases is not reached because the excess gas has already desorbed via low temperature pathways. However, atomic underlayers do not appear to template a low temperature desorption pathway in the ASW overlayer, which results in the observed burst peaks. This is further supported by the results in Fig. 5 where the Ar burst peak is suppressed when oxygen is co-deposited in the underlayer. The presence of O_2 opens the low temperature desorption pathway that acts as a "pressure" relief valve and thus removes the burst peak pathway.

The breakdown in diffusive-like behavior of the low temperature desorption feature for overlayers >300 ML observed in Figs. 6 and 7, can also be explained by the porosity in the overlayer. Initially, porous as-deposited ASW overlayers

provide a network of pathways for low temperature desorption, however, as the overlayer thickness increases the desorption peak is pushed to higher temperature. At these higher temperatures significant annealing of the porous ASW can occur resulting in larger pores.[36,37,39] Such annealing can create larger diameter pore channels allowing unfettered desorption of the gas that results in the peak temperature pile-up observed in Figs. 6 and 7. In this sense, the breakdown in diffusive behavior may not be the result of the overlayer thickness per se, but due to reaching a higher temperature. Eventually, annealing to even higher temperatures leads to the complete closure of the pores and thus the loss of the low temperature desorption pathway.[36,37,39]

In this (Paper II) and the preceding companion (Paper I) paper, we have thoroughly investigated the mechanisms for the release of trapped gases from underneath ASW films in two underlayer coverage regimes. In Paper I, the low coverage regime was investigated (~1 ML) and the primary release mechanism, the molecular volcano, was found to be due to a "top-down" crystallization-induced crack formation mechanism. The desorption behavior depends only on the crystallization and crack propagation kinetics of the ASW overlayer and is independent of the underlayer gas species. In Paper II, the high coverage regime was investigated (>1 ML) and two pre-crystallization desorption mechanisms were observed. Both are dependent on the particular underlayer species and as such represent "bottom-up" mechanisms. These works provide a physical, mechanistic explanation for the previous observational reports of gas release. Where possible (e.g., crystallization and crack propagation kinetics in Paper I and the pressure-induced desorption bursts in Paper II) a quantitative explanation has been given. However, beyond confirming that particular underlayers can affect the morphology of ASW overlayers (even for deposition at normal incidence), a quantitative physical explanation of morphologically driven desorption remains elusive. Nonetheless, it is clear that relatively small changes in the ASW overlayer (density, porosity) can give rise to dramatic differences in the release kinetics of the gaseous underlayer. Clearly, this is an important factor to consider when interpreting the experimental studies of gaseous release from laboratory analogs of astrophysical ices. Future work will focus on the surface structure of the underlayer and how it may induce porosity in the ASW overlayer.

ACKNOWLEDGMENTS

[1] R. May, R. Smith, and B. Kay, J. Chem. Phys. **138**, 104501 (2013).
[2] D. C. B. Whittet, Astrophys. J. **710**, 1009 (2010).
[3] A. H. Delsemme, J. Phys. Chem. **87**, 4214 (1983).
[4] A. Barnun, G. Herman, D. Laufer, and M. L. Rappaport, Icarus **63**, 317 (1985).
[5] A. Bar-Nun, J. Dror, E. Kochavi, and D. Laufer, Phys. Rev. B **35**, 2427 (1987).
[6] D. Laufer, E. Kochavi, and A. Bar-Nun, Phys. Rev. B **36**, 9219 (1987).
[7] A. Bar-Nun, I. Kleinfeld, and E. Kochavi, Phys. Rev. B **38**, 7749 (1988).
[8] R. L. Hudson and B. Donn, Icarus **94**, 326 (1991).
[9] P. Jenniskens and D. F. Blake, Science **265**, 753 (1994).
[10] P. Jenniskens and D. F. Blake, Astrophys. J. **473**, 1104 (1996).
[11] L. J. Allamandola, M. P. Bernstein, S. A. Sandford, and R. L. Walker, Space Sci. Rev. **90**, 219 (1999).
[12] A. Bar-Nun and D. Laufer, Icarus **161**, 157 (2003).
[13] G. Notesco, A. Bar-Nun, and T. Owen, Icarus **162**, 183 (2003).
[14] D. J. Burke and W. A. Brown, Phys. Chem. Chem. Phys. **12**, 5947 (2010).
[15] M. P. Collings, M. A. Anderson, R. Chen, J. W. Dever, S. Viti, D. A. Williams, and M. R. S. McCoustra, Mon. Not. R. Astron. Soc. **354**, 1133 (2004).
[16] R. Yokochi, U. Marboeuf, E. Quirico, and B. Schmitt, Icarus **218**, 760 (2012).
[17] R. S. Smith, C. Huang, E. K. L. Wong, and B. D. Kay, Phys. Rev. Lett. **79**, 909 (1997).
[18] R. S. Smith, C. Huang, E. K. L. Wong, and B. D. Kay, Surf. Sci. **367**, L13 (1996).
[19] R. J. Speedy, P. G. Debenedetti, R. S. Smith, C. Huang, and B. D. Kay, J. Chem. Phys. **105**, 240 (1996).
[20] R. S. Smith and B. D. Kay, Nature (London) **398**, 788 (1999).
[21] R. S. Smith, J. Matthiesen, J. Knox, and B. D. Kay, J. Phys. Chem. A **115**, 5908 (2011).
[22] R. S. Smith, N. G. Petrik, G. A. Kimmel, and B. D. Kay, Acc. Chem. Res. **45**, 33 (2012).
[23] P. Ayotte, R. S. Smith, K. P. Stevenson, Z. Dohnalek, G. A. Kimmel, and B. D. Kay, J. Geophys. Res., [Planets] **106**, 33387, doi:10.1029/2000JE001362 (2001).
[24] R. A. May, R. S. Smith, and B. D. Kay, Phys. Chem. Chem. Phys. **13**, 19848 (2011).
[25] R. A. May, R. S. Smith, and B. D. Kay, J. Phys. Chem. Lett. **3**, 327 (2012).
[26] E. A. Guggenheim, J. Chem. Phys. **13**, 253 (1945).
[27] K. S. Pitzer, J. Chem. Phys. **7**, 583 (1939).
[28] R. S. Smith, J. Matthiesen, and B. D. Kay, J. Chem. Phys. **133**, 174504 (2010).
[29] J. Matthiesen, R. S. Smith, and B. D. Kay, J. Chem. Phys. **133**, 174505 (2010).
[30] R. S. Smith, J. Matthiesen, and B. D. Kay, J. Chem. Phys. **132**, 124502 (2010).
[31] See supplementary material at http://dx.doi.org/10.1063/1.4793312 for several additional figures that are not necessary for an overall understanding of the scientific arguments presented here but may be of interest to some readers. Typically these figures make the same point as those in the main text but show results for other adsorbate molecules.
[32] K. P. Stevenson, G. A. Kimmel, Z. Dohnalek, R. S. Smith, and B. D. Kay, Science **283**, 1505 (1999).
[33] G. A. Kimmel, Z. Dohnalek, K. P. Stevenson, R. S. Smith, and B. D. Kay, J. Chem. Phys. **114**, 5295 (2001).
[34] G. A. Kimmel, K. P. Stevenson, Z. Dohnalek, R. S. Smith, and B. D. Kay, J. Chem. Phys. **114**, 5284 (2001).
[35] Z. Dohnalek, G. A. Kimmel, P. Ayotte, R. S. Smith, and B. D. Kay, J. Chem. Phys. **118**, 364 (2003).
[36] T. Zubkov, R. S. Smith, T. R. Engstrom, and B. D. Kay, J. Chem. Phys. **127**, 184707 (2007).
[37] T. Zubkov, R. S. Smith, T. R. Engstrom, and B. D. Kay, J. Chem. Phys. **127**, 184708 (2007).
[38] F. Cholette, T. Zubkov, R. S. Smith, Z. Dohnalek, B. D. Kay, and P. Ayotte, J. Phys. Chem. B **113**, 4131 (2009).
[39] R. S. Smith, T. Zubkov, Z. Dohnalek, and B. D. Kay, J. Phys. Chem. B **113**, 4000 (2009).
[40] Z. Dohnalek, G. A. Kimmel, D. E. McCready, J. S. Young, A. Dohnalkova, R. S. Smith, and B. D. Kay, J. Phys. Chem. B **106**, 3526 (2002).
[41] D. W. Flaherty, Z. Dohnalek, A. Dohnalkova, B. W. Arey, D. E. McCready, N. Ponnusamy, C. B. Mullins, and B. D. Kay, J. Phys. Chem. C **111**, 4765 (2007).
[42] D. W. Flaherty, R. A. May, S. P. Berglund, K. J. Stevenson, and C. B. Mullins, Chem. Mater. **22**, 319 (2010).
[43] R. A. May, D. W. Flaherty, C. B. Mullins, and K. J. Stevenson, J. Phys. Chem. Lett. **1**, 1264 (2010).